

Conditional Generative Modeling for Amorphous Multi-Element Materials

Honglin Li,^{1,2,*} Chuhao Liu,^{3,4,*} Yongfeng Guo,^{5,*} Xiaoshan Luo,^{1,*} Yijie Chen,^{6,*} Guangsheng Liu,⁷ Yu Li,² Ruoyu Wang,^{8,9} Zhenyu Wang,^{1,10} Jianzhuo Wu,⁵ Cheng Ma,¹ Zhuohang Xie,^{1,10} Jian Lv,¹ Yufei Ding,¹¹ Huabin Zhang,¹² Jian Luo,^{2,7} Zhicheng Zhong,^{8,9,13} Mufan Li,^{4,†} Yanchao Wang,^{1,‡} and Wan-Lu Li^{2,7,§}

¹Key Laboratory of Material Simulation Methods and Software of Ministry of Education,
College of Physics, Jilin University, Changchun, China

²Aiiso Yufeng Li Family Department of Chemical and Nano Engineering,
University of California, San Diego, La Jolla, CA, USA

³Institute of Molecular Engineering Plus, College of Chemistry, Fuzhou University, Fuzhou, China

⁴College of Chemistry and Molecular Engineering, Peking University, Beijing, China

⁵School of Physics, Nankai University, Tianjin, China

⁶Institute of Modern Physics, Fudan University, Shanghai, China

⁷Program in Materials Science and Engineering, University of California, San Diego, La Jolla, CA, USA

⁸School of Artificial Intelligence and Data Science,

University of Science and Technology of China, Hefei 230026, China

⁹Suzhou Institute for Advanced Research, University of Science and Technology of China, Suzhou 215123, China

¹⁰International Center of Future Science, Jilin University, Changchun, China

¹¹Department of Computer Science and Engineering,

University of California, San Diego, La Jolla, CA, USA

¹²Center for Renewable Energy and Storage Technologies, Physical Science and Engineering Division,
King Abdullah University of Science and Technology, Thuwal, Kingdom of Saudi Arabia

¹³Suzhou Lab, Suzhou 215123, China

Amorphous multi-element materials offer unprecedented tunability in composition and properties, yet their rational design remains challenging due to the lack of predictive structure-property relationships and the vast configurational space. Traditional modeling struggles to capture the intricate short-range order that dictates their stability and functionality. We here introduce ApolloX, a pioneering predictive framework for amorphous multi-element materials, establishing a new paradigm by integrating physics-informed generative modeling with particle swarm optimization, using chemical short-range order as an explicit constraint. By systematically navigating the disordered energy landscape, ApolloX enables the targeted design of thermodynamically stable amorphous configurations. It accurately predicts atomic-scale arrangements, including composition-driven metal clustering and amorphization trends, which are well-validated by experiments, while also guiding synthesis by leveraging sluggish diffusion to control elemental distribution and disorder. The resulting structural evolution, governed by composition, directly impacts catalytic performance, leading to improved activity and stability with increasing amorphization. This predictive-experimental synergy transforms the discovery of amorphous materials, unlocking new frontiers in catalysis, energy storage, and functional disordered systems.

I. Introduction

Materials science is increasingly moving towards computationally driven materials design, with crystal structure prediction (CSP), coupled with density functional theory (DFT) calculations, playing a critical role in this emerging paradigm[1–5]. Significant progress in CSP developments has led to numerous methodological advancements and successful applications. This has ushered in a new era where computational research drives the predictive discovery of novel materials with unexpected properties, offering essential insights to guide experimental synthesis. This is exemplified by the theory-driven discovery of high-temperature superconducting superhydrides[6–8].

Yet, such progress has largely been confined to materials with ordered crystal structures typically described by small unit cells. In contrast, the discovery of multi-element amorphous materials is still predominantly explored through trial-and-error experimental methods[9–11].

Due to the absence of translational symmetry and long-range order [12, 13], no simple unit cells can fully capture the nature of amorphous materials. A large simulated cell is typically required to model these materials, but this exceeds current computational capabilities due to the high computational cost of DFT approaches[14]. Furthermore, the disordered and metastable nature of amorphous materials makes their modeling the Achilles' heel of theoretical descriptions[9]. These challenges have created significant barriers, particularly for multi-elemental systems. As a result, the computationally driven design of amorphous materials remains in its infancy.

The key goal of computationally driven design of amorphous materials is to uncover the relationships between

* These authors contribute equally to this work.

† mufanli@pku.edu.cn

‡ wyc@calypso.cn

§ wal019@ucsd.edu

structure and properties using computational techniques. This involves modeling how the atomic-level structure of amorphous materials influences their macroscopic properties. Exploring amorphous materials starting from a crystalline structure is a common approach in theoretical research. The Molecular Dynamics (MD) simulation uses a crystalline configuration as the initial structure and applies conditions to obtain an amorphous structure for property analysis[15, 16]. Additionally, the Special Quasirandom Structure (SQS) method[17, 18], coupled with the Monte Carlo (MC) process, provides a strategy for constructing initial structures in smaller systems. However, accurately capturing the potential energy landscape of amorphous systems remains a challenge. The cluster expansion (CE) method, combined with DFT, is commonly employed in crystalline materials to identify low-energy states through structure enumeration and ground-state search, providing valuable insights into new strategies for studying amorphous materials[19–21].

However, applying these methods to complex multi-component amorphous systems is challenging, as increasing elemental diversity exponentially complicates atomic interactions and property predictions[9, 10, 22]. Furthermore, the inherent metastability of amorphous materials further limits conventional structure prediction. These challenges become particularly pronounced in systems with extreme compositions, such as high-entropy alloys and ceramics, highlighting the need for advancements in computational efficiency and predictive accuracy.

Here, we propose a physics-guided computational framework named ApolloX (Automatic Prediction by generative mOdel for Large-scaLe Optimization of X-composition materials) that integrates a conditional generative deep learning model[23] with particle swarm optimization (PSO)[24] for simulating multi-element amorphous materials. This framework harnesses chemical short-range order (CSRO)[25–27] descriptors, represented by Pair Density Matrices (PDMs), alongside thermodynamic insights from DFT and machine learning potentials (MLP)[28] to systematically generate structurally reasonable models of these complex disordered systems. Our approach not only predicts atomic arrangements that align with experimental observations but also reveals fundamental insights into composition-driven structural evolution and structure-function relationships. The strong agreement between predicted and experimental structures validates its ability to capture key atomic-scale features, including short-range ordering and progressive metal aggregation. Additionally, the model-informed synthesis strategy, guided by sluggish diffusion control, enables precise tuning of elemental distribution and amorphization trends. Our predicted FeCoNiMoBO_x materials exhibit enhanced catalytic performance for oxygen evolution reaction (OER) with increasing amorphization, validated by experiments. This predictive-experimental synergy establishes a transformative framework for designing amorphous multi-element material, surpassing conventional trial-and-error

methods.

II. Results and discussion

A. Physics-guided generative model with PSO

Amorphous materials, lacking translational symmetry and long-range order, are best characterized by their short-range order. Our method predicts these structures using only chemical composition and local thermodynamic information. Fig. 1A outlines the workflow of ApolloX, consisting of four main steps. Initially, the PDM was introduced as a descriptor of CSRO, capturing atomic nearest-neighbor interactions (Fig. 1B). It is constructed by selecting each atom as the center and counting the number of neighboring atoms within a sphere of radius r_{cut} . Each matrix element represents the count of a specific pair of neighboring atoms, capturing nearest-neighbor interactions among different element types. By classifying local atomic environments and reducing structural complexity, the PDM provides a powerful tool for analyzing amorphous materials. A training database was constructed with 10,000 randomly generated structures spanning a range of prototype configurations (e.g., FCC, BCC, HCP), and MLPs were used to optimize these structures, significantly reducing computational costs.

Next, the PDM-structure pairs served as training set for the conditional generative model. The model architecture, illustrated in Fig. 1C, integrates a conditional variational autoencoder with a diffusion framework (Cond-CDVAE) [23] to generate amorphous solid structures with the desired PDM. Compared to the original model, which was designed for the generation of crystal structures under high-pressure conditions, our modified Cond-CDVAE aims to establish the relationship between structures and their corresponding PDMs. The model first encodes the structure features into a latent space, and then decodes/generates a structure in a denoising score-matching manner. To achieve this, the vectorized PDM matrices are normalized and concatenated with composition representation vectors to form the conditional vectors used in both the training and generation stages.

The final step employs a population-based PSO algorithm[24] to refine the predicted structures. In each iteration, 100 structures are generated with a target PDM, relaxed to local minima, and assessed for thermodynamic stability using enthalpy of mixing and configurational entropy (Fig. 1D). The most stable structure’s PDM is then used to generate new candidates, iteratively refining configurations toward thermodynamically favorable states. The PYSWARMS package[29] (Fig. 1E) facilitates these PSO iterations. To maintain structural diversity and avoid local minima, 60% of energy-ranked structures are carried over to the next cycle, while 40% are newly generated. This iterative process continues until a predefined termination criterion is met, ensuring an op-

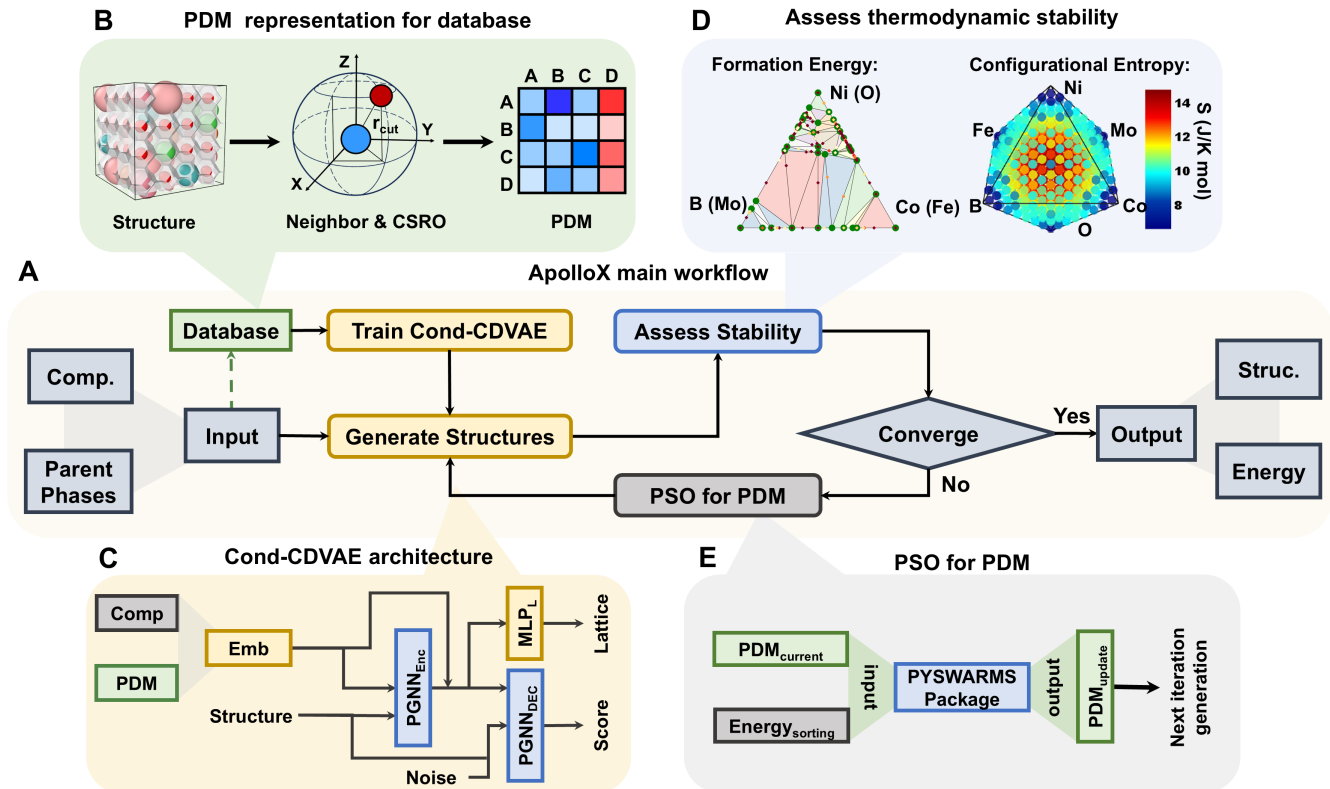


FIG. 1. **Overview workflow of ApolloX.** (A) Main workflow of ApolloX for structural modeling, including the model’s iterative generation process. (B) Structures are represented using the Pair Density Matrix (PDM), and a dataset is constructed by mapping each structure to its corresponding PDM. (C) The model architecture of the Cond-CDVAE. An embedding network (EMB) integrates a structure’s composition (Comp.) and PDM into a unified conditioning vector. The graph neural network encoder (PGNN_{Enc}) encodes the structure alongside its conditioning vector into a latent vector, capturing its underlying features. Subsequently, a multi-layer perceptron MLP_L predicts the lattice parameters based on the latent vector. And the graph neural network decoder (PGNN_{Dec}) outputs a score function for denoising and reconstruction of a plausible structure. (D) Enthalpy stability is evaluated using the convex hull method, and entropy stability is assessed based on configurational entropy. (E) PSO is employed to optimize the PDM, using the PYSWARMS package.

timized exploration of the amorphous energy landscape.

B. Validating ApolloX for amorphous materials discovery

To evaluate the effectiveness of ApolloX, we applied it to $\text{Fe}_{12}\text{Co}_{12}\text{Ni}_{12}\text{Mo}_{12}\text{B}_{12}\text{O}_{60}$ containing 120 atoms, a multi-component system incorporating elements commonly used in OER catalysts[30–32]. Boric oxide (BO_x) establishes a uniform microenvironment[33], eliminating distinct crystal phases and interfacial boundaries due to electron deficiency of boron[34], while transition metals introduce diverse local coordination environments. This system serves as an optimal platform for evaluating ApolloX’s predictive accuracy in thermodynamic stability, short-range order, and structure-function relationships in complex disordered materials.

A total of 10,000 candidate structures of $\text{Fe}_{12}\text{Co}_{12}\text{Ni}_{12}\text{Mo}_{12}\text{B}_{12}\text{O}_{60}$ were generated by ran-

domly substituting elements in an FCC parent phase within a $3 \times 4 \times 5$ supercell. These structures were then systematically relaxed using the DPA-2 framework[28] with model fine-tuning. Subsequently, the PDMs of the relaxed structures were utilized to train the Cond-CDVAE model. To assess the accuracy of our PDM-driven Cond-CDVAE model, we selected a reference PDM as the target and generated 100 structures. As illustrated in Fig. 2A, the average differences between the generated and target PDMs for most element pairs are below 25%, demonstrating the high accuracy of our Cond-CDVAE generative model in capturing the targeted CSRO characteristics.

To demonstrate the capabilities of ApolloX in structure search for amorphous systems, an initial set of 100 structures was generated, followed by structural evolution via PSO over 15 generations. The evolution of the lowest-energy structure across generations during PSO was shown in Fig. 2B, with the thermodynamically most favorable configuration shown in

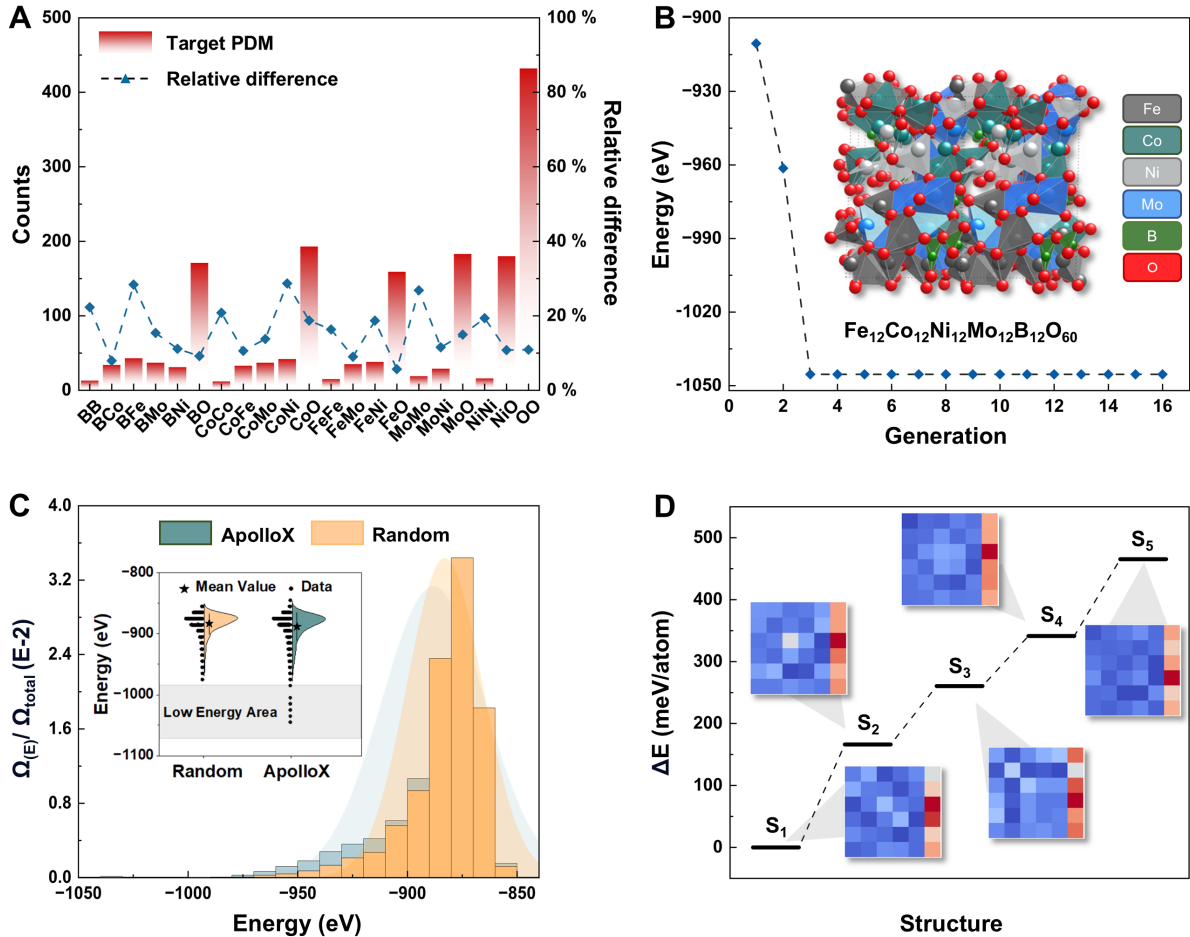


FIG. 2. **Model prediction of structural energy distribution and analysis.** (A) PDM target and the relative difference of the generated structures, illustrating the model’s high accuracy in capturing short-range ordering effects. (B) Iteration results of the PSO algorithm, where the model identifies the minimum-energy structure in the third generation. One of the thermodynamically stable structures is also shown. (C) The energy distribution of structures generated by both the ApolloX and Random methods is analyzed. A bar chart illustrates how these structures are distributed across different energy intervals, revealing a higher density of ApolloX-generated structures at lower energy levels. In the inset, a violin plot highlights the global mean energy and the distribution of structures within the low-energy range, spanning from -990 eV to -1050 eV. (D) The five lowest-energy structures were identified by ApolloX. The PDMs for these structures, shown in the inset, exhibit a unique short-range ordering pattern.

the inset. Obviously, the lowest-energy structure of amorphous $\text{Fe}_{12}\text{Co}_{12}\text{Ni}_{12}\text{Mo}_{12}\text{B}_{12}\text{O}_{60}$, with an energy of -1045.39 eV, emerged in the third generation, demonstrating the efficiency of the PSO algorithm in optimizing PDMs. Furthermore, the ApolloX method significantly outperformed the Random approach, as evidenced by the fact that the average energy achieved by ApolloX (-888.21 eV) was notably lower than that of the Random approach (-882.93 eV). This result underscores the superior performance of our Cond-CDVAE model in generating thermodynamically favorable amorphous structures.

To further validate the efficiency of ApolloX, we compared 1,500 structures generated by the Random method with those obtained using our ApolloX approach. The energies of all structures were systematically evaluated

using the fine-tuned DPA-2 model. The results in Fig. 2C confirm the superior capability of ApolloX in generating low-energy structures, as evidenced by the fact that within the energy range below -960 eV, ApolloX-generated structures accounted for 75.2%, significantly outperforming the Random method (24.8%). It is noteworthy that the Random method fails to generate any structures in the low-energy region below -990 eV, whereas five structures produced by ApolloX fall within this range. Further analysis of the five lowest-energy structures predicted by ApolloX reveals significant structural diversity and notable variations in CSRO within these configurations. (Fig. 2D). These findings not only highlight the effectiveness of ApolloX in generating low-energy configurations but also demonstrate its capability

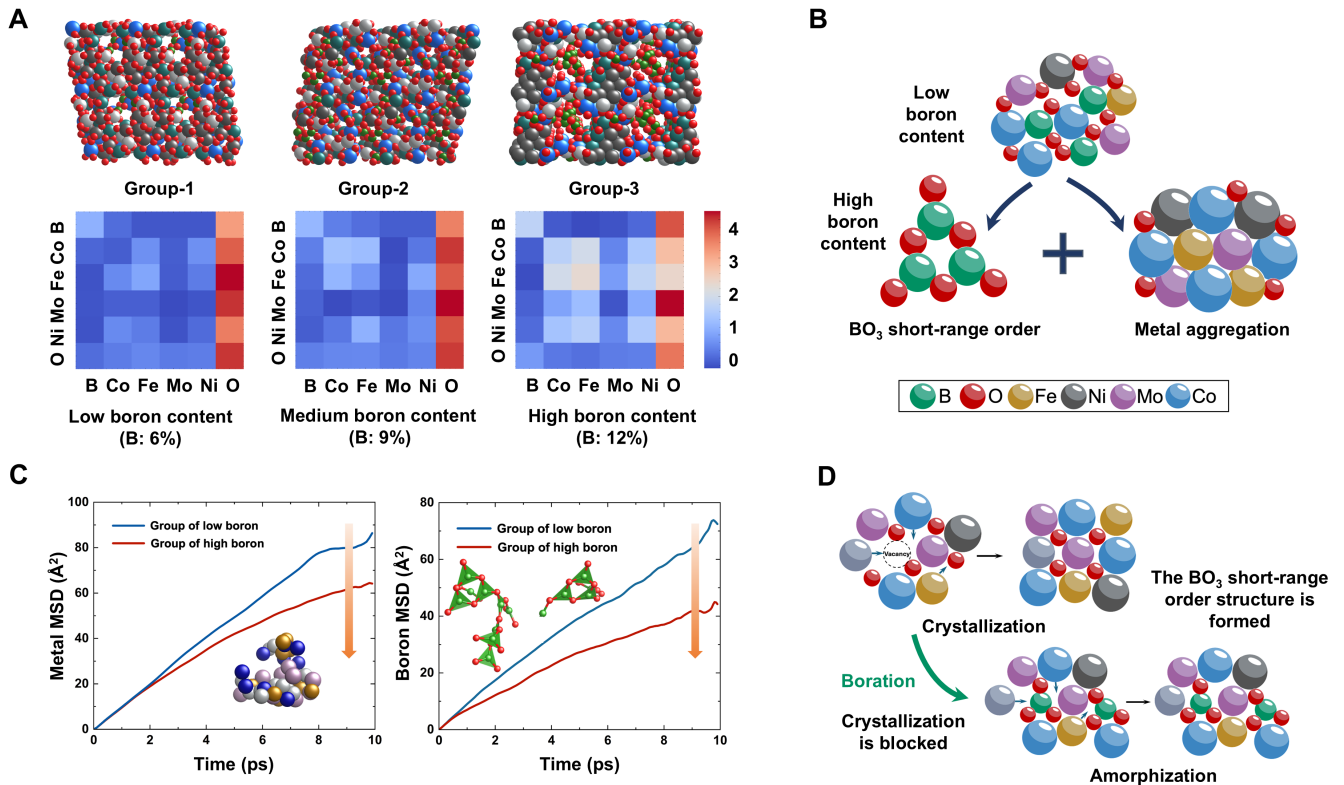


FIG. 3. **Short-range order evolution and diffusion-limited amorphization mechanism.** (A) A heatmap from theoretical modeling shows the atomic nearest-neighbor relationships in structures with three different boron contents. (B) Atomic distribution models reveal that higher boron content promotes the formation of short-range ordered B–O bonding, accompanied by metal clustering. (C) A comparison of diffusion rates for metals and boron within the same system indicates that boron diffuses significantly slower than metals. (D) As boron content increases, the formation of BO₃ motifs becomes more pronounced, suppressing overall atomic mobility, hindering lattice rearrangement, and facilitating amorphization.

to strike an adequate balance between exploration and exploitation in predicting approximate structures within complex amorphous material systems.

Although the theoretical foundations of the CE method suggest that it may not be suitable for amorphous systems, we assessed its applicability for a balanced comparison with our workflow, using the CE approach implemented in the ATAT software[35] for structure modeling and energy prediction[21]. As expected, the fitting results of Fe₁₂Co₁₂Ni₁₂Mo₁₂B₁₂O₆₀ indicate that the amorphous system does not produce convergent cluster model fits with acceptable accuracy (0.02 eV as suggested by ATAT). Detailed information can be found in Supplementary Materials. This issue arises from the high concentration of non-metallic atoms, which causes lattice distortion and results in an amorphous structure. In contrast, our approach demonstrates enhanced capabilities for structural search and energy prediction in amorphous systems, underscoring its potential advantages over the CE method.

C. Boron-driven structural evolution and ordering

To examine the influence of boron content on microstructure and material properties, we employed ApolloX to generate structures with 6%, 9%, and 12% boron for Group-1, -2 and -3, respectively, while maintaining equivalent metal ratios. For each composition, 10,000 structures were generated to identify the thermodynamically most stable configuration, incorporating both configurational entropy and enthalpy. We then extracted the CSROs of the lowest-energy structures for further analysis. Fig. 3A shows the predicted structures and elemental enrichment heat maps, where increasing boron content shifts metal distribution from dispersed to aggregated. Notably, our model captures only local short-range ordering effects; thus, the observed atomic clustering does not necessarily correlate with long-range amorphization.

A comparison of atomic-level structures across the three groups reveals a clear transition in CSRO with increasing boron content. In Group-1 (low boron), metal-O-metal connectivity dominates. As boron content increases, oxygen preferentially bonds with boron rather

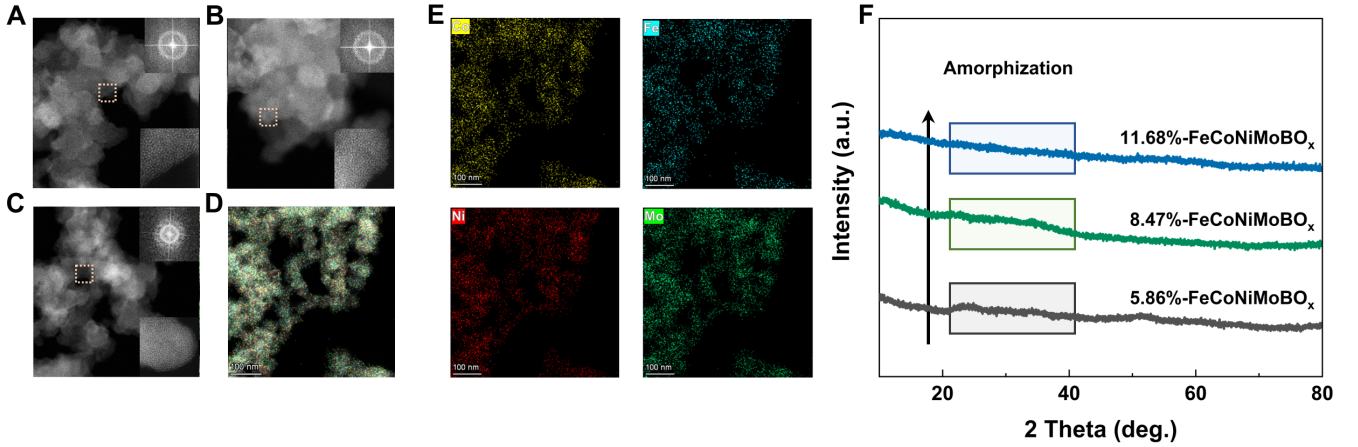


FIG. 4. **Experimental characterization of the amorphous structure of FeCoNiMoBO_x materials.** (A to C) HAADF-STEM images of Groups-1, 2, and 3, with corresponding FFT-SAED patterns (top) confirming the amorphous nature and aberration-corrected images (bottom) highlighting atomically dispersed metal sites. (D) Overlapped EDS mapping on a HAADF-STEM image showing homogeneous elemental distribution in Group-3. (E) STEM elemental mapping for Group-3. (F) XRD patterns of Groups 1-3, demonstrating increasing amorphization with higher boron content.

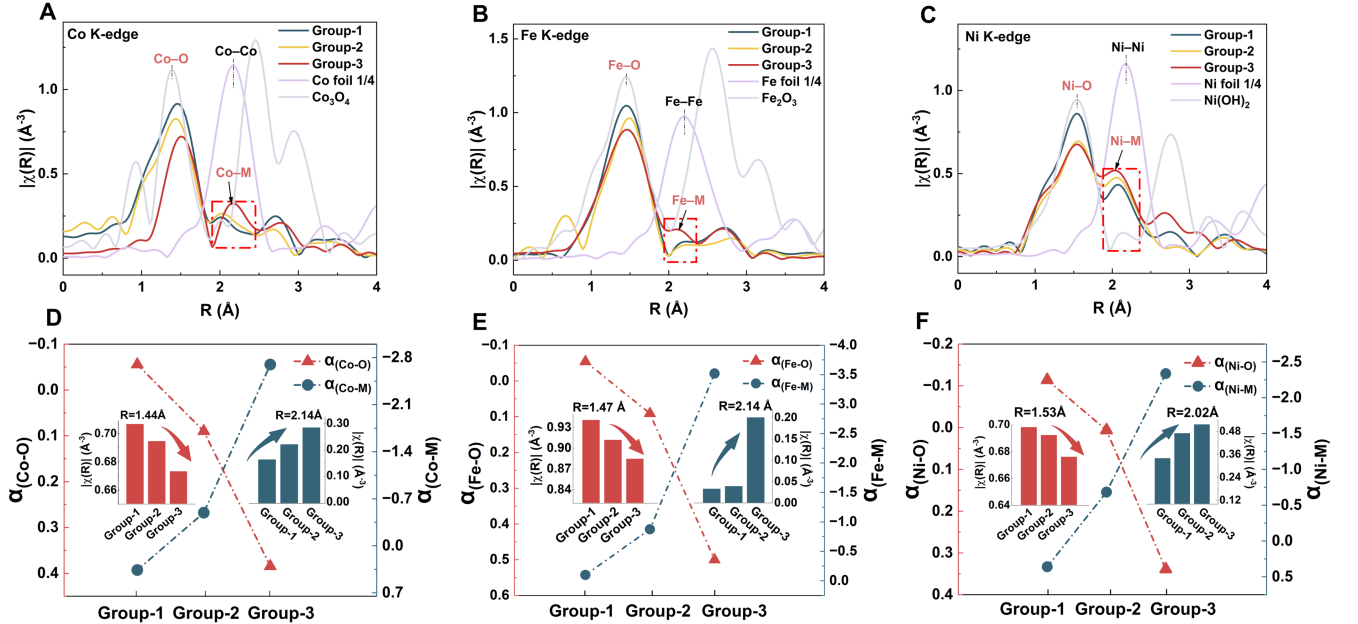


FIG. 5. **Structural characterization and interaction analysis.** (A to C) Fourier-transformed EXAFS spectra of Fe, Co, and Ni K-edges in R-space. (D to F) α_{ij} values for M-O and M-M (M = Co, Fe, Ni) interactions derived from predicted structures of FeCoNiMoBO_x in three groups, compared with the magnitude of $|\chi|(R)$ from EXAFS. Positive α_{ij} values indicate dispersion, while negative values correspond to aggregation.

than metals, forming BO_3 motifs (Fig. 3B), where boron coordinates with three oxygen atoms, introducing local short-range ordering. In Group-3 (highest boron content), this shift toward BO_3 formation leads to reduced metal-oxygen interactions and enhanced metal clustering (Fig. 3A). These findings highlight the significant role of boron in modifying local CSRO, driving a shift from metal-O-metal connectivity toward B-O coordina-

tion and direct metal-metal interactions.

D. Diffusion-limited amorphization mechanism

In 2024, Hsu *et al.*[36] proposed that in multi-component materials, the element with the lowest diffusion rate governs lattice restructuring kinetics and influ-

ences the structural disorder. To investigate this effect, we performed MD simulations on molten microstructures with varying boron concentrations (Fig. 3C). Our results indicate a systematic decrease in the overall diffusion rates with increasing boron content (fig. S6). Further analysis revealed that boron atoms diffuse significantly more slowly than metal constituents, with their diffusion rate declining more sharply as boron concentration increases.

Our results also showed that higher boron concentrations promote the formation of BO_3 units, effectively increasing the local “damping volume”. In contrast to most multi-element oxide materials, which typically exhibit crystalline order, such B-O coordination suppresses oxygen diffusivity shown in fig. S6 and alters the crystallization dynamics of the system, as illustrated in Fig. 3D. These findings suggest that boron acts as the rate-limiting element in atomic mobility, thereby impeding crystallization. As boron content increases, the system’s tendency toward amorphization becomes more pronounced.

E. From theoretical design to experimental insights

Inspired by boron’s sluggish diffusion and strong B-O interactions, we developed a synthesis strategy for multi-element amorphous materials by incorporating metal atoms into a BO_x framework. Guided by predicted compositions, this approach produced amorphous FeCoNiMoBO_x with controlled boron gradients (5.86%, 8.74%, and 11.68%; table S2). High-resolution high-angle annular dark field scanning transmission electron microscopy (HAADF-STEM) images (Fig. 4 A-C) confirm the amorphous morphology while EDS mapping (Fig. 4D,E) shows uniform elemental distribution. The absence of crystalline diffraction spots in the fast Fourier transform selected area electron diffraction (FFT-SAED) patterns (Fig. 4A–C, top insets) and XRD analysis (Fig. 4F) further supports the amorphous structure. Additionally, spherical aberration-corrected HAADF-STEM images (Fig. 4A–C, bottom insets) reveal atomically dispersed metal atoms without lattice fringes. These results validate our synthesis strategy, demonstrating that sluggish diffusion stabilizes amorphous structures with tunable compositions. The structural disorder of amorphous materials limits direct differentiation among the three FeCoNiMoBO_x groups via electron microscopy. However, XRD analysis (Fig. 4F) shows progressively smoother diffraction patterns with increasing boron content, consistent with our generative model predicting greater structural disorder at higher boron concentrations.

The extended X-ray absorption fine structure (EXAFS) shown in Fig. 5 provided further information on the local coordination environment. The Co K-edge spectra (Fig. 5A) confirmed the absence of Co-Co or Co-O-Co bonds seen in crystalline Co foil and Co_3O_4 , respectively,

instead showing predominant Co-O coordination at ~ 1.4 Å. As boron content increased, Co-O peak intensity decreased while Co-M (M = metal) interactions at ~ 2.2 Å intensified, indicating progressive metal aggregation. Similar trends were observed for Ni and Fe K-edges (Fig. 5B,C). Structural predictions further quantified this transition using α_{ij} values[37] (Fig. 5D–F), where increasing α_{ij} for M-O and decreasing values for M-M interactions confirmed a shift toward metal aggregation, validating our predictive model.

The structural evolution directly influences catalytic performance. Multi-elemental oxides are widely studied for catalysis and energy storage due to their structural adaptability, electronic tunability, and suppressed cation diffusion, which enhance stability and activity[38–43]. Amorphous oxides, in particular, often outperform crystalline counterparts due to their enhanced electronic flexibility and active site accessibility[44, 45]. Leveraging these advantages, we examined the OER activity of amorphous FeCoNiMoBO_x , integrating the catalytic properties of Fe/Co/Ni oxides with boron’s role in electronic modulation[41, 46, 47]. Given the correlation between Co e_g orbital occupancy and OER activity,[48, 49] we employed the λ_1/λ_2 descriptor—validated for multi-element oxides[50]—to assess the impact of boron content. As shown in fig. S7, both λ_1 and λ_2 values for Co ions systematically increase with boron concentration, indicating enhanced OER activity at higher boron levels. Linear sweep voltammetry confirmed this trend (fig. S8): while overpotentials at 10 mA cm^{-2} were similar across all groups (229 mV, 225 mV, and 222 mV for Groups 1–3), at 100 mA cm^{-2} , they decreased significantly with increasing boron content (515 mV, 483 mV, and 456 mV), aligning with theoretical predictions.

Additionally, in situ Raman spectroscopy shown in fig. S9 confirmed the amorphous nature of the catalysts, showing no detectable metal oxide vibrations (e.g., E_{2g} , A_{1g}) and a dominant $-\text{OH}$ peak at 773 cm^{-1} persisting across applied potentials, indicating structural stability. The high-boron-content catalyst (Group-3) was integrated into an anion exchange membrane water electrolyzer, exhibiting a low voltage degradation rate of 0.227 mV h^{-1} over 800 hours, significantly outperforming IrO_2 (0.9 mV h^{-1} , fig. S9).

These results demonstrate that increasing boron content enhances both OER activity and durability in FeCoNiMoBO_x . Boron incorporation reduces diffusion, improving stability by mitigating metal corrosion (Fig. 3C). Additionally, higher boron concentrations promote metal aggregation (Fig. 5), forming metal-metal bonds that modulate local coordination environments and intermediate binding energies. The observed increase in Co-Co bonding at lower binding energies ($< -920 \text{ eV}$) (fig. S3) and enhanced Co-Ni/Co clustering, evidenced by α_{ij} (Fig. 5D), may further contribute to improved catalytic activity.

III. Conclusions

This work represents a paradigm shift in the computational design of amorphous multi-element materials by integrating a physics-guided generative model with PSO algorithm. By encoding CSRO and thermodynamic stability into the generative process, our approach transcends conventional trial-and-error methods, enabling predictive synthesis of complex disordered systems. The ability to rationally design amorphous structures at atomic level with high thermostability was validated through the synthesis and characteriza-

tion of FeCoNiMoBO_x, where the predicted amorphization trends, metal clustering effects, and functional enhancements were experimentally confirmed. Moving forward, this framework opens the door to property-driven materials design, where desired functionalities dictate atomic configurations, accelerating the discovery of next-generation materials for catalysis, energy storage, and beyond.

References

-
- [1] S. M. Woodley, R. Catlow, Crystal structure prediction from first principles. *Nat. Mater.* **7**, 937–946 (2008).
- [2] Y. Wang, J. Lv, L. Zhu, Y. Ma, CALYPSO: A method for crystal structure prediction. *Comput. Phys. Commun.* **183**, 2063–2070 (2012).
- [3] Y. Wang, J. Lv, L. Zhu, Y. Ma, Crystal structure prediction via particle-swarm optimization. *Phys. Rev. B* **82**, 094116 (2010).
- [4] A. R. Oganov, A. O. Lyakhov, M. Valle, How Evolutionary Crystal Structure Prediction Works—and Why. *Acc. Chem. Res.* **44**, 227–237 (2011).
- [5] K. Ryan, J. Lengyel, M. Shatruk, Crystal Structure Prediction via Deep Learning. *J. Am. Chem. Soc.* **140**, 10158–10168 (2018).
- [6] H. Wang, J. S. Tse, K. Tanaka, T. Iitaka, Y. Ma, Superconductive sodalite-like clathrate calcium hydride at high pressures. *Proc. Natl. Acad. Sci. U.S.A.* **109**, 6463–6466 (2012).
- [7] H. Liu, I. I. Naumov, R. Hoffmann, N. W. Ashcroft, R. J. Hemley, Potential high- T_c superconducting lanthanum and yttrium hydrides at high pressure. *Proc. Natl. Acad. Sci. U.S.A.* **114**, 6990–6995 (2017).
- [8] F. Peng, *et al.*, Hydrogen Clathrate Structures in Rare Earth Hydrides at High Pressures: Possible Route to Room-Temperature Superconductivity. *Phys. Rev. Lett.* **119**, 107001 (2017).
- [9] Y. Liu, A. Madanchi, A. S. Anker, L. Simine, V. L. Deringer, The amorphous state as a frontier in computational materials design. *Nat. Rev. Mater.* **10**, 228–241 (2025).
- [10] Y. Yao, *et al.*, High-entropy nanoparticles: Synthesis-structure-property relationships and data-driven discovery. *Science* **376**, eabn3103 (2022).
- [11] L. Banko, *et al.*, Combinatorial materials discovery strategy for high entropy alloy electrocatalysts using deposition source permutations. *arXiv e-prints* p. DOI:10.48550/arXiv.2106.08776 (2021).
- [12] J. Miao, P. Ercius, S. J. L. Billinge, Atomic electron tomography: 3D structures without crystals. *Science* **353**, aaf2157 (2016).
- [13] Y. Yuan, *et al.*, Three-dimensional atomic packing in amorphous solids with liquid-like structure. *Nat. Mater.* **21**, 95–102 (2022).
- [14] C. Chang, V. L. Deringer, K. S. Katti, V. Van Speybroeck, C. M. Wolverton, Simulations in the era of exascale computing. *Nat. Rev. Mater.* **8**, 309–313 (2023).
- [15] I. Štich, R. Car, M. Parrinello, Amorphous silicon studied by ab initio molecular dynamics: Preparation, structure, and properties. *Phys. Rev. B* **44**, 11092–11104 (1991).
- [16] J. Akola, R. O. Jones, Structural phase transitions on the nanoscale: The crucial pattern in the phase-change materials Ge₂Sb₂Te₅ and GeTe. *Phys. Rev. B* **76**, 235201 (2007).
- [17] A. Zunger, S.-H. Wei, L. G. Ferreira, J. E. Bernard, Special quasirandom structures. *Phys. Rev. Lett.* **65**, 353–356 (1990).
- [18] A. van de Walle, *et al.*, Efficient stochastic generation of special quasirandom structures. *Calphad* **42**, 13–18 (2013).
- [19] R. Drautz, Atomic cluster expansion for accurate and transferable interatomic potentials. *Phys. Rev. B* **99**, 014104 (2019).
- [20] N. A. Zarkevich, D. D. Johnson, Reliable First-Principles Alloy Thermodynamics via Truncated Cluster Expansions. *Phys. Rev. Lett.* **92**, 255702 (2004).
- [21] A. van de Walle, Multicomponent multisublattice alloys, nonconfigurational entropy and other additions to the Alloy Theoretic Automated Toolkit. *Calphad* **33**, 266–278 (2009).
- [22] R. Singh, A. Sharma, P. Singh, G. Balasubramanian, D. D. Johnson, Accelerating computational modeling and design of high-entropy alloys. *Nat. Comput. Sci.* **1**, 54–61 (2021).
- [23] X. Luo, *et al.*, Deep learning generative model for crystal structure prediction. *npj Comput. Mater.* **10**, 254 (2024).
- [24] J. Kennedy, R. Eberhart, Particle swarm optimization, in *Proceedings of ICNN'95 - International Conference on Neural Networks* (IEEE,1995), pp. 1942–1948.
- [25] M. Sakata, N. Cowlam, H. Davies, Chemical short-range order in liquid and amorphous Cu₆₆Ti₃₄ alloys. *J. Phys. F: Met. Phys.* **11**, L157 (1981).
- [26] X. Chen, *et al.*, Direct observation of chemical short-range order in a medium-entropy alloy. *Nature* **592**, 712–716 (2021).
- [27] C. Saw, R. Schwarz, Chemical short-range order in dense random-packed models. *J. Less-Common Met.* **140**, 385–393 (1988).
- [28] D. Zhang, *et al.*, DPA-2: a large atomic model as a multi-task learner. *npj Comput. Mater.* **10**, 293 (2024).
- [29] L. J. Miranda, PySwarms: a research toolkit for Particle Swarm Optimization in Python. *J. Open Source Softw.* **3**, 433 (2018).

- [30] B. Zhang, *et al.*, Homogeneously dispersed multimetal oxygen-evolving catalysts. *Science* **352**, 333–337 (2016).
- [31] G. Chen, *et al.*, Two orders of magnitude enhancement in oxygen evolution reactivity on amorphous $\text{Ba}_{0.5}\text{Sr}_{0.5}\text{Co}_{0.8}\text{Fe}_{0.2}\text{O}_{3-\delta}$ nanofilms with tunable oxidation state. *Sci. Adv.* **3**, e1603206 (2017).
- [32] B. Zhang, *et al.*, High-valence metals improve oxygen evolution reaction performance by modulating 3d metal oxidation cycle energetics. *Nat. Catal.* **3**, 985–992 (2020).
- [33] G. Ferlat, A. P. Seitsonen, M. Lazzeri, F. Mauri, Hidden polymorphs drive vitrification in B_2O_3 . *Nat. Mater.* **11**, 925–929 (2012).
- [34] W.-L. Li, *et al.*, From planar boron clusters to borophenes and metalloborophenes. *Nat. Rev. Chem.* **1**, 0071 (2017).
- [35] A. van de Walle, M. Asta, G. Ceder, The alloy theoretic automated toolkit: A user guide. *Calphad* **26**, 539–553 (2002).
- [36] W.-L. Hsu, C.-W. Tsai, A.-C. Yeh, J.-W. Yeh, Clarifying the four core effects of high-entropy materials. *Nat. Rev. Chem.* **8**, 471–485 (2024).
- [37] J. M. Cowley, An Approximate Theory of Order in Alloys. *Phys. Rev.* **77**, 669–675 (1950).
- [38] J. Suntivich, K. J. May, H. A. Gasteiger, J. B. Goodenough, Y. Shao-Horn, A perovskite oxide optimized for oxygen evolution catalysis from molecular orbital principles. *Science* **334**, 1383–1385 (2011).
- [39] T. A. Batchelor, *et al.*, High-entropy alloys as a discovery platform for electrocatalysis. *Joule* **3**, 834–845 (2019).
- [40] L. Han, *et al.*, Multifunctional high-entropy materials. *Nat. Rev. Mater.* **9**, 846–865 (2024).
- [41] Z. Xiao, *et al.*, Operando identification of the dynamic behavior of oxygen vacancy-rich Co_3O_4 for oxygen evolution reaction. *J. Am. Chem. Soc.* **142**, 12087–12095 (2020).
- [42] T. Löffler, *et al.*, Design of complex solid-solution electrocatalysts by correlating configuration, adsorption energy distribution patterns, and activity curves. *Angew. Chem. Int. Ed.* **59**, 5844–5850 (2020).
- [43] J.-T. Ren, L. Chen, H.-Y. Wang, Z.-Y. Yuan, High-entropy alloys in electrocatalysis: from fundamentals to applications. *Chem. Soc. Rev.* **52**, 8319–8373 (2023).
- [44] P. Thangavel, G. Kim, K. S. Kim, Electrochemical integration of amorphous NiFe (oxy)hydroxides on surface-activated carbon fibers for high-efficiency oxygen evolution in alkaline anion exchange membrane water electrolysis. *J. Mater. Chem. A* **9**, 14043–14051 (2021).
- [45] J. Park, S. Lee, S. Kim, Recent advances in amorphous electrocatalysts for oxygen evolution reaction. *Front. Chem.* **10**, 1030803 (2022).
- [46] Z.-W. Gao, *et al.*, Engineering NiO/NiFe LDH intersection to bypass scaling relationship for oxygen evolution reaction via dynamic tridimensional adsorption of intermediates. *Adv. Mater.* **31**, 1804769 (2019).
- [47] Z.-P. Wu, X. F. Lu, S.-Q. Zang, X. W. Lou, Non-noble-metal-based electrocatalysts toward the oxygen evolution reaction. *Adv. Funct. Mater.* **30**, 1910274 (2020).
- [48] X. Wang, *et al.*, Electrospun thin-walled CuCo_2O_4 @C nanotubes as bifunctional oxygen electrocatalysts for rechargeable Zn–air batteries. *Nano Lett.* **17**, 7989–7994 (2017).
- [49] Z. Jin, *et al.*, Rugged high-entropy alloy nanowires with in situ formed surface spinel oxide as highly stable electrocatalyst in Zn–air batteries. *ACS Mater. Lett.* **2**, 1698–1706 (2020).
- [50] F. Fan, *et al.*, Applicable Descriptors under Weak Metal–Oxygen d–p Interaction for the Oxygen Evolution Reaction. *Angew. Chem. Int. Ed.* p. e202419718 (2024).
- [51] N. Norman, B. E. Warren, X-Ray Measurement of Short Range Order in Ag–Au. *J. Appl. Phys.* **22**, 483–486 (1951).
- [52] V. Blum, G. L. W. Hart, M. J. Walorski, A. Zunger, Using genetic algorithms to map first-principles results to model Hamiltonians: Application to the generalized Ising model for alloys. *Phys. Rev. B* **72**, 165113 (2005).
- [53] G. Kresse, J. Furthmüller, Efficient iterative schemes for ab initio total-energy calculations using a plane-wave basis set. *Phys. Rev. B* **54**, 11169–11186 (1996).
- [54] A. H. Larsen, *et al.*, The atomic simulation environment—a Python library for working with atoms. *J. Phys.: Condens. Matter* **29**, 273002 (2017).
- [55] M. Ångqvist, *et al.*, ICET – A Python Library for Constructing and Sampling Alloy Cluster Expansions. *Adv. Theor. Simul.* **2**, 1900015 (2019).
- [56] J. Gasteiger, J. Groß, S. Günnemann, Directional Message Passing for Molecular Graphs, in *International Conference on Learning Representations (ICLR)* (2020).
- [57] J. Gasteiger, S. Giri, J. T. Margraf, S. Günnemann, Fast and Uncertainty-Aware Directional Message Passing for Non-Equilibrium Molecules, in *Advances in Neural Information Processing Systems (NeurIPS)* (2020).
- [58] J. Gasteiger, F. Becker, S. Günnemann, GemNet: Universal Directional Graph Neural Networks for Molecules, in *Advances in Neural Information Processing Systems (NeurIPS)* (2021).

Acknowledgements

This work was supported by the National Natural Science Foundation of China (Grants No. T2225013, No. 12034009, No. 12174142, No. 42272041, No. 22372004), National Key Research and Development Program of China (Grants No. 2022YFA1402304, No. 2024YFA1509500), Beijing Natural Science Foundation No. Z240027, Program for Jilin University Science and Technology Innovative Research Team (2021TD-05), Program for Jilin University Computational Interdisciplinary Innovative Platform. Part of the calculation was performed in the high-performance computing center of Jilin University. Part of the calculation was performed in the San Diego Super-computer Center (SDSC) Expanse at UC San Diego through allocation MAT240028 from the Advanced Cyberinfrastructure Coordination Ecosystem: Services & Support (ACCESS) program. W.-L.L. and H.Z. thank the KAUST Supercomputing Laboratory for providing computational resources on the Shaheen III supercomputer through project k10175.

Author contributions M.L., Y.W., and W.-L.L. supervised the research and project. H.L. designed the workflow of ApolloX. C.L., H.Z., and J.L. performed the experimental component, including synthesis, characterization, and performance testing. Y.G., X.L., J.L., and Y.D. contributed to code development and model design, while Y.C. and J.W. analyzed and interpreted the

data, conducted performance evaluations, and performed model comparisons. G.L. and Y.L. carried out catalytic property calculations. R.W., Z.W., and Z.Z. contributed to training the machine learning potential. Additionally, H.L., C.L., M.L., Y.W., W.-L.L., X.L., C.M., and Z.X. contributed to the writing of the manuscript.

Competing interests: The authors declare no competing interests.

Data and code availability: The authors declare that the main data supporting the findings of this study are contained within the paper and its associated Supplementary Information. The ApolloX source code is available on GitHub (<https://github.com/FNC001/ApolloX>)

Additional information

Supplementary information The online version contains supplementary material available at XXX.

Correspondence and requests for materials should be addressed to Mufan Li, Yanchao Wang or Wan-Lu Li.

Supplementary Information

This PDF file includes:

Materials and Methods
 Figures S1 to S9
 Tables S1 to S2

Materials and Methods

Construction of the PDM descriptor

From a thermodynamic perspective, the thermal stability of multi-element materials is governed by the interplay between the mixing enthalpy (ΔH_{mix}) and the mixing entropy (ΔS_{mix}). This relationship can be described by the Gibbs free energy equation:

$$\Delta G_{\text{mix}} = \Delta H_{\text{mix}} - T \cdot \Delta S_{\text{mix}} \quad (\text{S1})$$

where ΔG_{mix} is the mixing Gibbs free energy, T is the temperature, and ΔH_{mix} and ΔS_{mix} are the mixing enthalpy and mixing entropy, respectively.

In multi-element materials, the uniform distribution of constituent elements increases the configurational entropy (ΔS_{mix}), thereby lowering the Gibbs free energy (ΔG_{mix}) and enhancing the overall thermodynamic stability. As the number of elements in the system rises, ΔS_{mix} increases accordingly, so incorporating more elements typically boosts the mixing entropy and stabilizes the alloy.

However, for structures with the same composition (i.e., identical configurational entropy), the mixing enthalpy (ΔH_{mix}) becomes the primary determinant of thermodynamic stability. Since the formation enthalpy of chemical bonds between different elements (H_{ij}) can vary significantly, the specific interactions among elements play a crucial role in influencing ΔH_{mix} , thereby affecting the overall stability of the material.

Warren-Cowley SRO parameter

To describe the local environment of multi-element materials, the Warren-Cowley SRO parameter[37, 51] is often defined as:

$$\alpha_{ij}(r) = 1 - \frac{P_{ij}(r)}{c_j}, \quad (\text{S2})$$

where i, j denote atomic species; $P_{ij}(r)$ is the conditional probability of finding an atom of type j at distance r (or within a specific neighbor shell) around a central atom of type i ; and c_j is the overall molar (or atomic) fraction of species j in the system.

If $\alpha_{ij}(r) = 0$, it indicates that the distribution of species j around species i matches the global composition; if $\alpha_{ij}(r) > 0$, it implies that species j is deficient (repelled) around species i ; if $\alpha_{ij}(r) < 0$, it implies that species j is enriched (aggregated) around species i .

In an ideal random distribution, $\alpha_{ij}(r) = 0$ for any i, j , and r . When the system exhibits short-range order, $\alpha_{ij}(r)$ deviates from 0.

Comparative modeling of amorphous multi-element materials

For comparison with ApolloX, a disordered model was constructed using the special quasi-random structure (SQS) method[17] and implemented via the Alloy Theoretic Automated Toolkit (ATAT) package[21]. For the bulk phase, random distributions of two-, three-, and four-body clusters were considered, with the cutoff distances set to the third-nearest neighbor for two-body clusters, and to the nearest neighbor for both three- and four-body clusters.

The cluster expansion (CE) procedure[19] was performed using the ATAT package as well. In the CE approach, crystalline materials are modeled using a generalized Ising model in which various multibody cluster interaction terms, called effective cluster interactions (ECIs)[52], must be determined. In the CE method, the energy of a HEA configuration can be calculated as:

$$E(\vec{\sigma}) = \sum_{\alpha} J_{\alpha} m_{\alpha} \langle \Gamma_{\alpha} \cdot (\vec{\sigma}) \rangle \tag{S3}$$

where α denotes a cluster, m_{α} represents the number of symmetry-equivalent clusters α , J_{α} are the concentration-independent ECIs. The cluster functions $\langle \Gamma_{\alpha} \cdot (\vec{\sigma}) \rangle$ are defined as the product of point functions occupying positions on a particular cluster α . We employed 2,500 randomly disordered initial bulk phase configurations (containing 120 atoms), constructed using the aforementioned SQS method. These configurations were optimized for relaxation using a trained machine learning potential (MLP) to facilitate the fitting of CE algorithm.

Model details of Cond-CDVAE

The initial training set of 10,000 structures was generated by randomly occupying atomic sites in fixed-lattice structures. These configurations are then optimized using a finetuned DPA-2[28], a machine-learning potential capable of handling a wide range of elements. After optimization, each structure is labeled by its PDM.

We adapted the Cond-CDVAE model to generate structures conditioned on the PDM. In our scenario, the conditioning variables include both composition and PDM. The element type of each atom is represented by a categorical embedding vector. The composition is then calculated as a weighted average of the element type embedding vectors based on the number of atoms of each type. Meanwhile, the PDM, represented as a matrix of continuous variables, is flattened into a vector and normalized in the training set. The composition vector and PDM vector are concatenated to form the conditional vector. Other model hyperparameters are provided in Table S1. Once trained, Cond-CDVAE[23] can generate new structures conditioned on the specified PDM, offering a versatile framework to explore diverse CSRO configurations in high-entropy materials.

During the generation stage, the target composition and PDM should be provided. These conditioning variables, combined with a latent vector sampled from the latent space, are used by the lattice predictor to predict lattice parameters. Subsequently, the PGNN_{Dec} reconstructs a valid structure from random atomic coordinates using Langevin dynamics.

DFT and MD calculations

In DFT calculations, the Perdew Burke-Ernzerhof generalized gradient approximation and projector-augmented wave (PAW) pseudopotentials implemented in VASP code[53] were employed. For Fe, Co, Ni, Mo, and B, the number of valence electrons of 8, 9, 10, 6, and 3 were explicitly considered, respectively. The corresponding valence electron configurations are Fe ($3d^6 4s^2$), Co ($3d^7 4s^2$), Ni ($3d^8 4s^2$), Mo ($4d^4 5s^2$), and B ($2s^2 2p^1$), which are in agreement with the ZVAL values obtained from our pseudopotential setup. Core electrons were treated using PAW potentials. The cutoff energy of 650 eV and the Monkhorst–Pack k -points spacing as Γ for sampling the Brillouin zone were used for structure optimizations to reach the energy and force convergence criteria of 1 meV/atom and 10 meV/Å, respectively.

To refine the generated structures, we fine-tune the pretrained DPA-2 model[28] with selected MD trajectories frames to achieve both accuracy and efficiency in searching for local minima. Geometry optimization with L-BFGS method implemented in ASE package[54] was employed to relax each candidate structure into a DPA-2-based local minima. The fitness function for these simulations was the free energy at $T = 0$ K, which reduces to enthalpy, ensuring the physical relevance of the predicted configurations. Although local optimization increases computational cost, it reduces noise in the energy landscape, improves configuration comparability and produces optimized structures for subsequent analysis.

Finetune details of DPA-2

The structural complexity of the $B_{12}Mo_{12}Co_{12}Fe_{12}Ni_{12}O_{60}$ system poses significant challenges for structure optimization using first-principles methods. While MLPs have emerged as a promising approach to accelerate quantum

mechanical calculations, enabling high-throughput, large-scale, and long-timescale atomic simulations at a significantly reduced computational cost, their accuracy and transferability critically depend on the quality of the training set. However, generating training data from scratch is both computationally expensive and labor-intensive, and MLPs often struggle to generalize beyond the scope of their training data. To address these limitations, we fine-tune the pre-trained universal DPA-2 model[28], which employs a universal descriptor trained on a diverse dataset computed at different levels of theory and can be further adapted to specific chemical systems of interest. The DPA-2 descriptor consists of a repinit layer to embed the local atomic environment with a cutoff radius of 6.0 Å; the atomic representation is subsequently updated using six message-passing repformer layers. Specifically, we refine the DPA-2 model using trajectories obtained from *ab-initio* MD simulations consisting of 2789 frames under a *random* branch, whose fitting network consists of three hidden layers with 240 neurons each. After 80000 training steps, the resulting model achieves a root mean square error (RMSE) of 7.76 meV/atom in energy, 139.61 meV/Å in force, and 0.068 meV/atom in virial, demonstrating its efficacy in accurately describing the targeted system.

Normalized variance of PDM

To investigate the chemical short-range order of the structure, we first computed the variance of atomic pairs in the PDM across different energy ranges. This variance reflects the uniformity and consistency of atomic pair coordination within specific energy ranges. Specifically, atomic pairs with smaller variances exhibit better coordination consistency within a given energy range. Atomic pairs that retain smaller variances in low-energy regions are likely to play a significant role in the structural stability, while atomic pairs with larger variances demonstrate greater spatial dispersion and may contribute less to structural stability.

Actually, the variance of atomic pair coordination numbers is also correlated with their mean values. To simplify the comparison of the relative consistency of atomic pair coordination numbers, we use the variance-to-mean ratio for subsequent statistical analysis. For structures across all energy ranges, the variance-to-mean ratios of different atomic pairs are shown in fig. S2. Oxygen-oxygen pairs are excluded due to their significantly larger variance, which would affect the observation of other atom pairs.

PDM is classified into self-pair interactions, intermetallic pairs, and metal-oxygen interactions. The variance-to-mean ratio of the PDM in the energy ranges below and above -920 eV is shown in fig. S3. It can be observed that, regardless of whether the energy is less than or greater than -920 eV, the variance of self-pair interactions is always smaller than that of intermetallic pairs, which in turn is smaller than that of metal-oxygen pairs. However, the relative ordering of these three atomic pair groups varies across different energy ranges. For the more stable structures with energies below -920 eV, it is notable that some Ni-X pairs (such as Ni-Ni, Fe-Ni, and B-Ni), as well as B-B pairs, have relatively small coordination number variances, suggesting that these atomic pairs may play a crucial role in forming stable structures and significantly impact the chemical short-range order of the structure.

Cluster expansion analysis

The high compositional complexity of the system involving six elements presents significant challenges because of the intricate interactions and vast configurational space. In smaller atomic systems, atomic interactions may not be fully captured, and the enumeration of configurations becomes stagnant. As the number of atoms in the system up to six, the configurational space grows exponentially, complicating the structure search process. To address this challenge, we utilized a set of fixed-concentration disordered models constructed using the SQS structural relaxation method to provide input energies. A $3 \times 4 \times 5$ supercell containing 120 atoms was employed, and a total of 2,500 structures were considered in the analysis. As illustrated in fig. S4A, the fitted LOOCV scores persist at a high level (0.095 eV), exceeding the accuracy threshold suggested by ATAT (0.02 eV). Additionally, increasing the diameter of the two-body clusters or incorporating three-body clusters leads to an even higher CV score. For CE fitting, the two-body cluster with the lowest LOOCV score (cutoff = 5.5 Å) was selected and fitted using the least-squares method to obtain the ECI for further testing. Subsequent five-fold cross-validation performed with the scikit-learn method yielded a root mean squared error (RMSE) of approximately 0.09 eV, as shown in (fig. S4B). And the predicted energies (fig. S4C) exhibit poor agreement with an R^2 value of only 0.1, which is markedly lower than the typical accuracy achieved for alloys with crystalline structures. This poor fitting primarily arises from the significant displacement of non-metallic atoms during structural relaxation, which disrupts the BCC symmetry of the system, as depicted in fig. S4D–E. Therefore, for amorphous high-entropy materials with a substantial concentration of non-metallic atoms, accurately predicting lattice site occupancy and cluster energies using the CE method is challenging.

In addition to the least-squares fitting method, two additional fitting methods were also employed to test the cluster expansion based on the selected SQS structures. Fig. 5 shows the two-body cluster truncation radius tests for Lasso

and Ridge fitting, with RMSE values for both methods exceeding 0.09 eV (fig. S5A–B).

Furthermore, by scanning the hyperparameter alpha for these two methods using the same two-body cluster truncation radius (5.5 Å) as the least squares fitting, it was found that the RMSE values converge near 0.1 eV (S5c–d), which is slightly higher than the least-squares fitting results via ATAT. Note that the Lasso and Ridge fitting were conducted using the ICET package [55]. Similar results obtained from these two additional methods indicate that their fitting performance is comparable to that of the least squares method, further suggesting that the amorphous high-entropy ceramic systems studied in this paper are not suitable for investigation via cluster expansion methods.

Diffusion rate analysis

The diffusion rate (D) can be inferred from the slope of the MSD curve, which can be calculated as:

$$\langle (r(t) - r(0))^2 \rangle = 6Dt \quad (\text{S4})$$

As the boron content increases, the overall diffusion rate of the system decreases, as shown in fig. S6A. This trend is also observed for metal and boron species (Fig. 3C in the main text) and oxygen components (fig. S6B). Additionally, oxygen atoms exhibit higher diffusion rates compared to metals and boron, with boron being the most sluggish component. Consequently, boron plays a key role in determining the crystallization rate, which in turn influences the degree of amorphization.

Catalytic descriptor calculation

The unoccupied d-band state parameter (λ_1) and the active d-band state parameter (λ_2) for Co ions are employed to characterize, respectively, the degree of unoccupied d-band states at active sites and the number of active states available for electron transfer. These parameters are essential for evaluating the oxygen evolution reaction (OER) performance of FeCoNiMoBO_x catalysts with varying boron (B) content. Specifically, λ_1 and λ_2 are calculated by integrating the projected density of states (PDOS) corresponding to the relevant electronic bands, as follows:

$$\begin{aligned} \lambda_1 &= N_{\text{Co}3d_{\text{unoccupied}}} + \frac{N_{\text{Co}d_{x^2-y^2}, d_{z^2}_{\text{unoccupied}}}}{N_{\text{O}2p_{\text{unoccupied}}}}, \\ \lambda_2 &= N_{\text{Co}3d} \times \frac{N_{\text{Co}d_{x^2-y^2}, d_{z^2}_{\text{unoccupied}}}}{N_{\text{O}2p_{\text{unoccupied}}}}, \end{aligned} \quad (\text{S5})$$

where $N_{\text{Co}3d}$, $N_{\text{Co}3d_{\text{unoccupied}}}$, $N_{\text{Co}d_{x^2-y^2}, d_{z^2}_{\text{unoccupied}}}$, and $N_{\text{O}2p_{\text{unoccupied}}}$ represent, respectively, the total number of states in the Co 3d band, the number of unoccupied states in the Co 3d band, the number of unoccupied states specifically within the Co $d_{x^2-y^2}$ and d_{z^2} orbitals, and the number of unoccupied states in the O 2p band. The parameter λ_1 quantifies the extent of unoccupied d-band states at Co active sites; higher λ_1 values indicate fewer electrons occupying the d-band and lower d-band electron energy levels, facilitating electron transfer from adsorbates to metal active sites and thereby reducing OER overpotential. Meanwhile, the parameter λ_2 quantifies the number of active d-band states at the Co site capable of participating in electron transfer interactions with the O 2p orbital under conditions of weak metal–oxygen interaction. Higher λ_2 values indicate a greater number of active states available for electron transfer, also leading to a reduction in OER overpotential.

Synthesis method of FeCoNiMoBO_x

Equimolar amounts of Fe(NO₃)₃, Co(NO₃)₂, Ni(NO₃)₂, and (NH₄)₆Mo₇O₂₄ (ammonium molybdate) were first prepared and dissolved in an equal volume of solvent to achieve a final concentration of 0.2 M, after which the solution was stored at 4 °C. Meanwhile, a 5 M NaBH₄ solution was prepared and refrigerated under the same conditions for 72 hours.

Subsequently, the metal salt solutions were combined in an ice bath, and a 5 M NaBH₄ solution, with twice the total volume of the metal salt solution, was rapidly added under vigorous stirring while maintaining the ice bath throughout the process. After reaction times of 3, 6, and 18 hours, three distinct catalysts, designated as Group-1, -2, and -3 FeCoNiMoBO_x, were obtained.

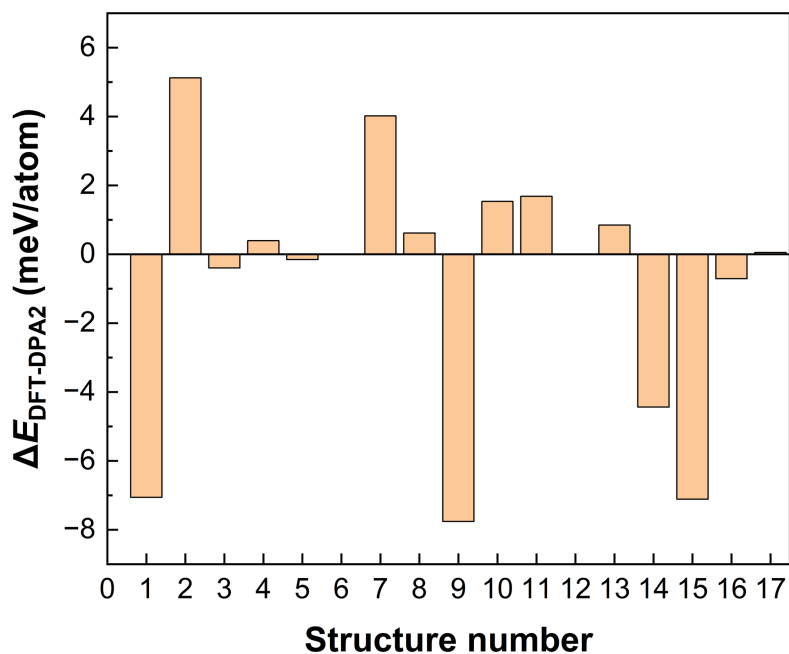


FIG. S1. **Accuracy analysis of DPA-2.** Compared the energy differences between DFT and DPA-2 for structures within different energy intervals to evaluate the accuracy of the MLP. The horizontal axis represents the number of structures, while the vertical axis shows the energy discrepancy between DFT and DPA-2 for each respective structure.

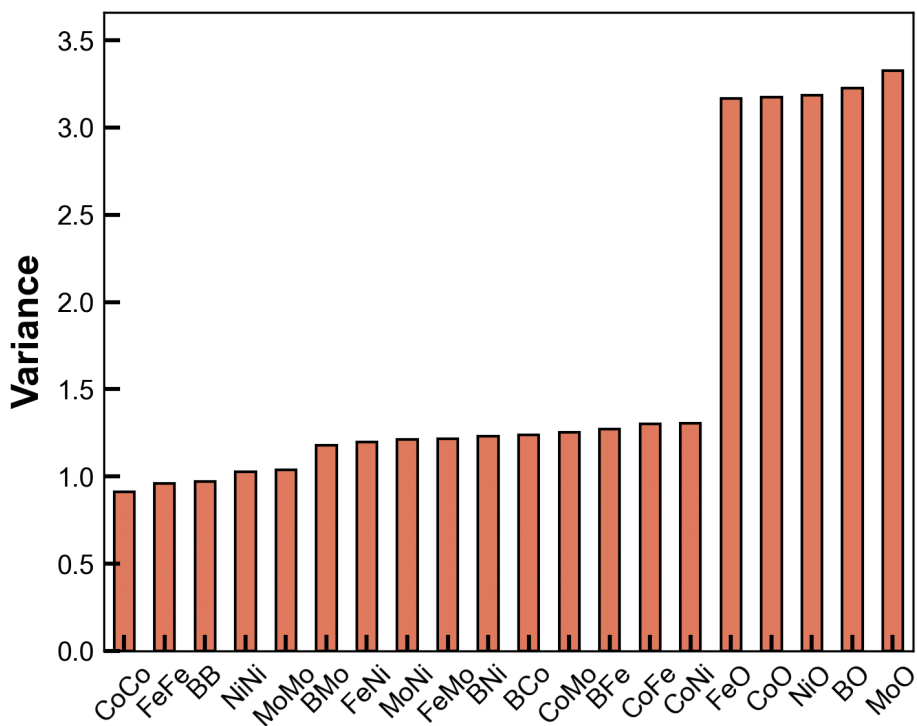


FIG. S2. **Variance-to-mean ratio of PDM** across all energy ranges.

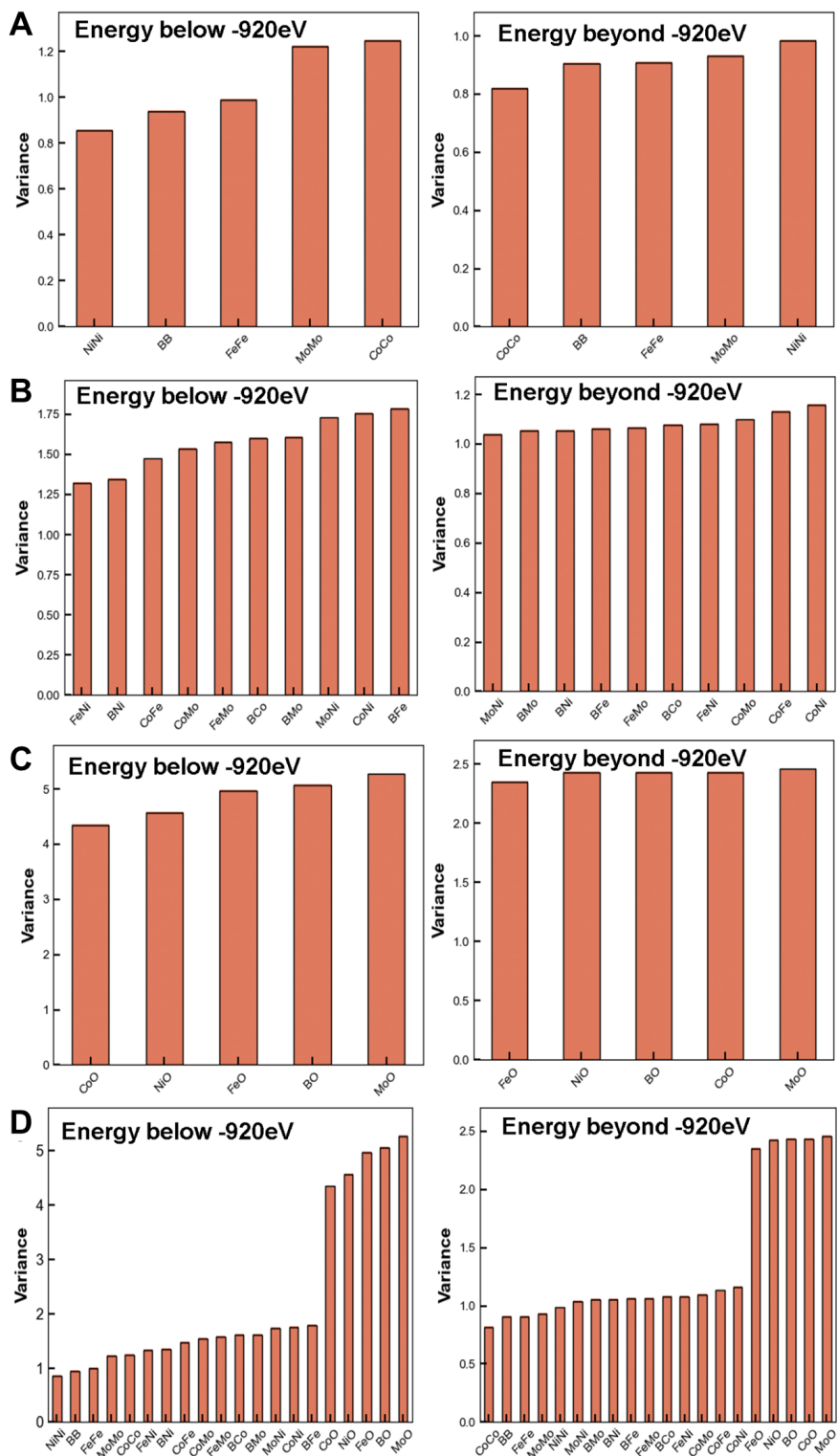


FIG. S3. **Normalized variance analysis of pair distributions.** (A) Variance of elemental pairs. (B) Variance of inter-metallic pairs. (C) Variance of metal-oxygen pairs. (D) Variance of all elements in the pair distribution matrix. The variance is normalized by dividing it by the corresponding mean value.

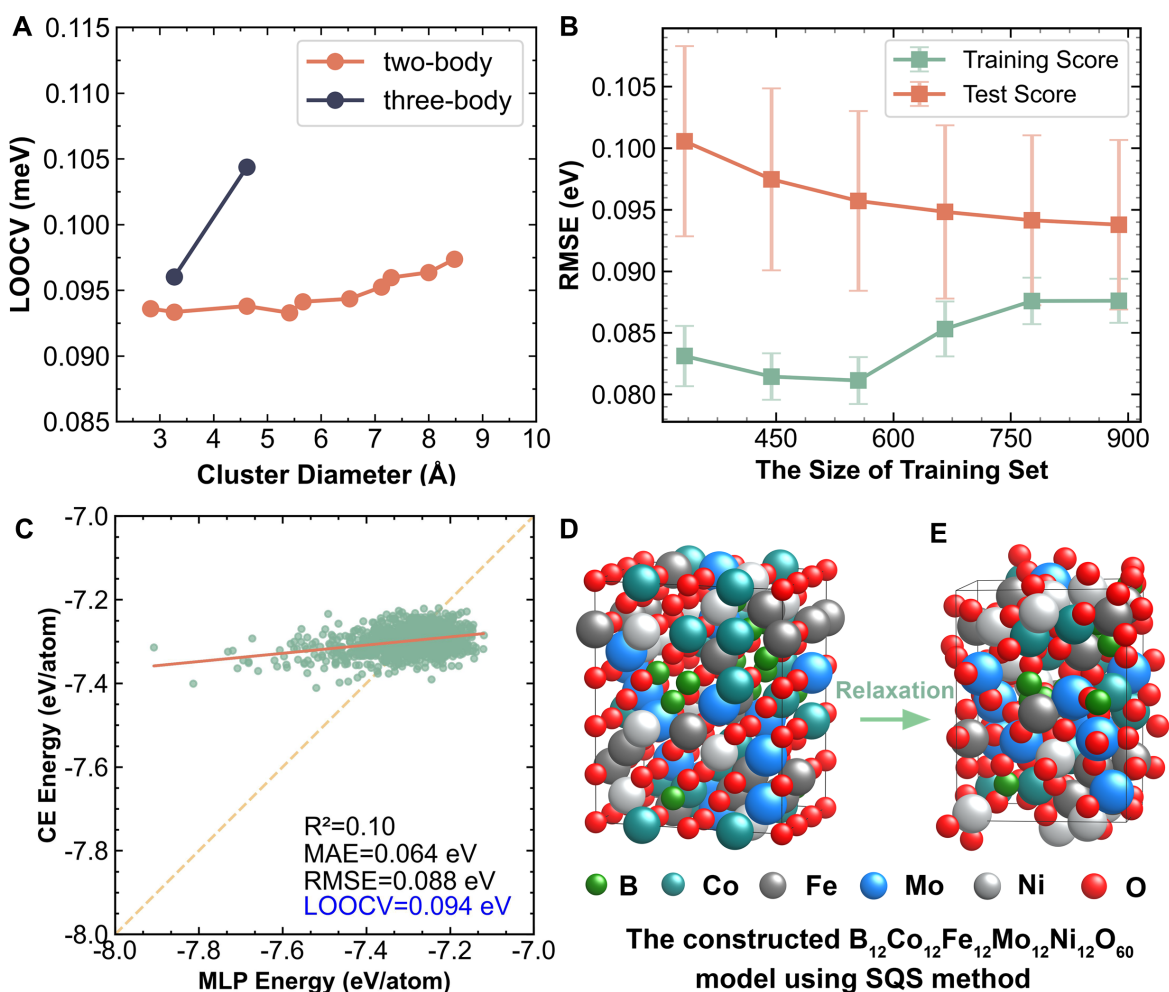


FIG. S4. The fitting information of clusters expansion using ATAT program. (A) The leave-one-out cross validation (LOOCV) scores for the test cluster diameters. All LOOCV scores exceed the acceptable values (0.02 eV) recommended by ATAT, nevertheless, the cluster corresponding to the lowest LOOCV score (a cutoff distance of 5.5 Å for two-body clusters) was selected for ECI fitting. (B) Learning curves for the selected model with least-squares fitting of ECIs. (C) Comparison between input energies obtained via MLP relaxation and the predicted energies from the CE model. (D–E) One of the states of SQS configuration before and after relaxation used for fitting the ECIs, with the amount of distortion annotated as 0.0128 by ATAT.

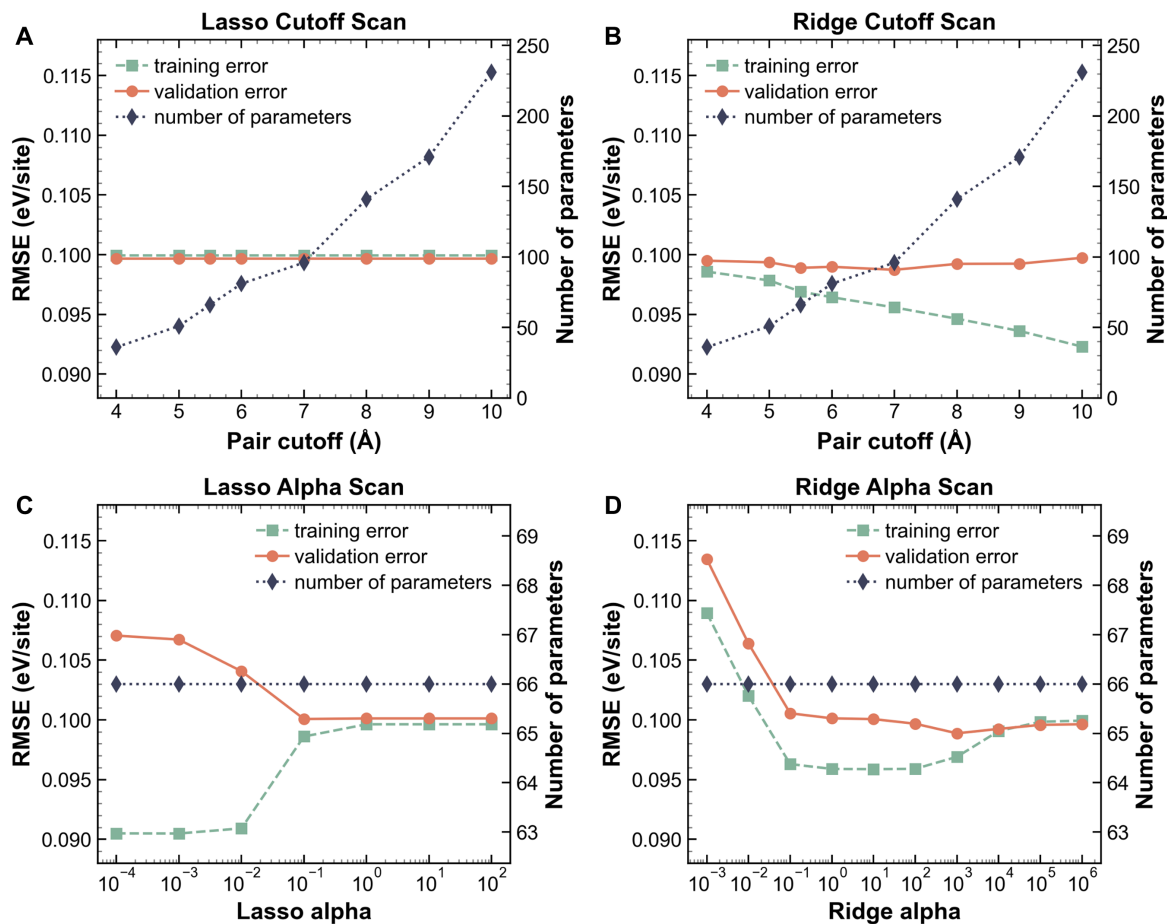


FIG. S5. **The cluster expansion fitting method using ICET package.** (A) The cluster diameter test of two-body (pair) clusters fitting with lasso method. (B) The cluster diameter test of two-body (pair) clusters fitting with ridge method. (C) The hyperparameter scan of lasso method. (D) The hyperparameter scan of ridge method.

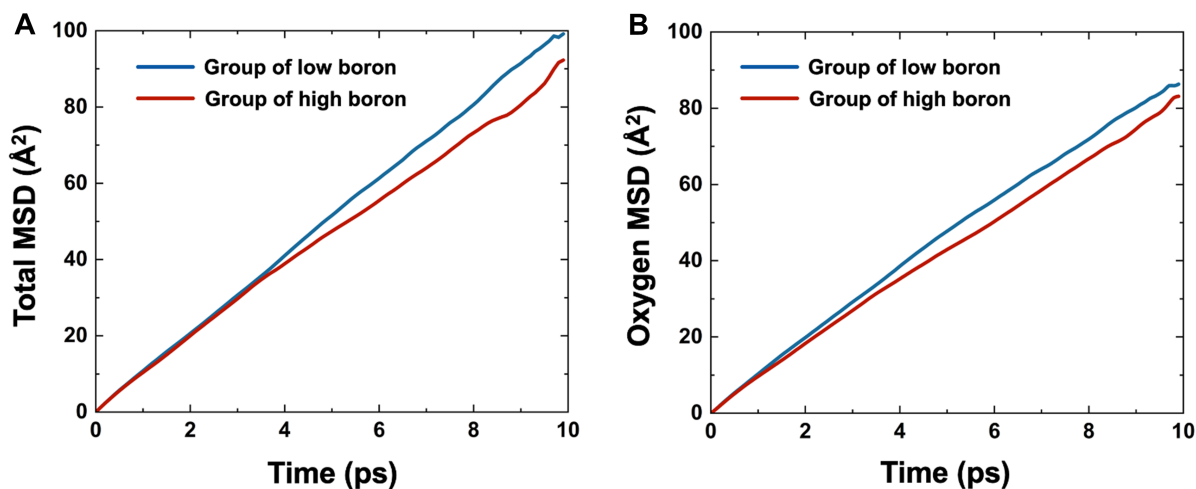


FIG. S6. Diffusion rate analysis across groups with different boron contents. **a** Total Mean Squared Displacement (MSD) of all elements. **b** MSD of oxygen atoms.

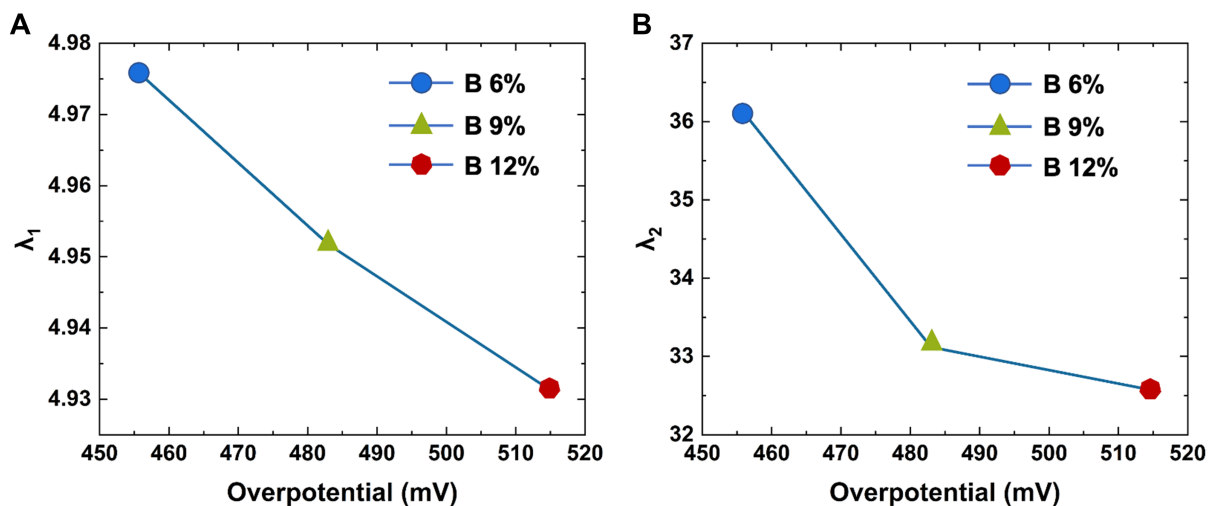


FIG. S7. Catalytic descriptor calculation. (A) Calculated λ_1 and (B) λ_2 values for Co in relation to experimentally measured OER overpotentials in FeCoNiMoBO_x catalysts across three groups with varying boron (B) content (6%, 9%, and 12%). The calculation method is described in the recent study on multi-element oxides for OER performance.[50]

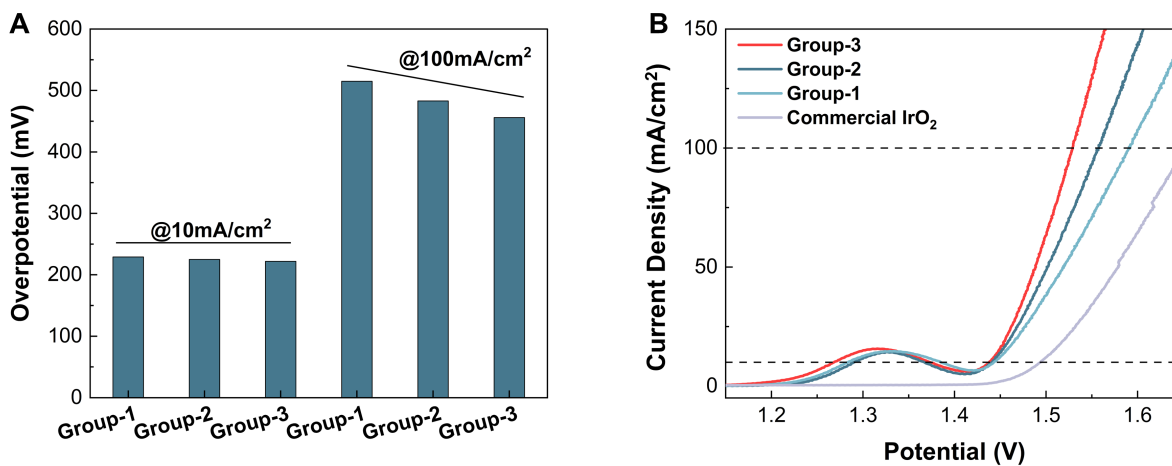


FIG. S8. **Catalytic performance.** (A) OER overpotentials across different groups at varying current densities. (B) Linear sweep voltammetry curves of Group-1, -2, and -3, compared with commercial IrO₂.

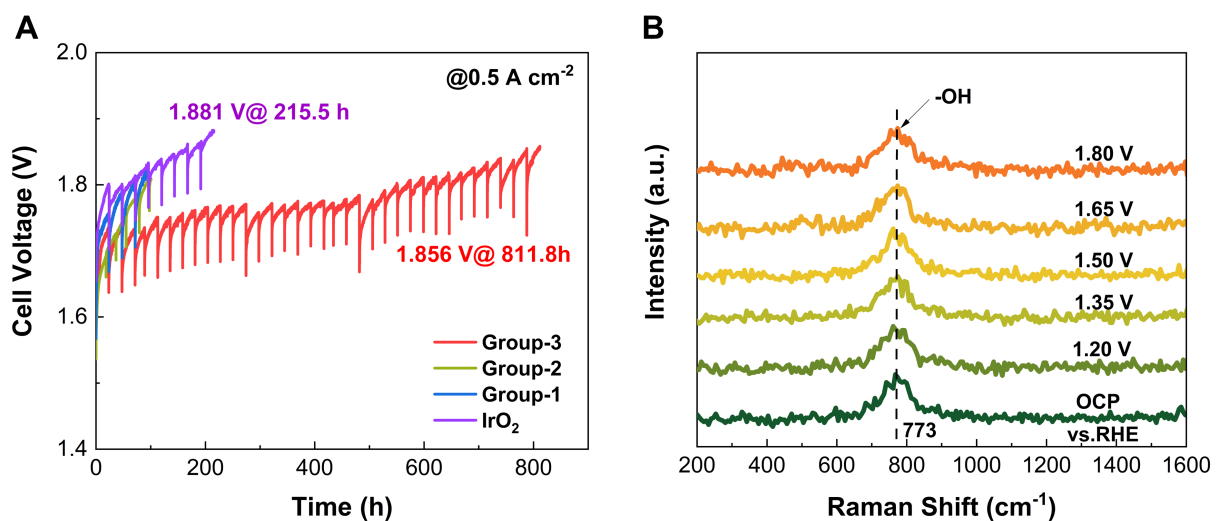


FIG. S9. **Catalytic stability.** (A) Stability test at 0.5 A/cm² using an anion exchange membrane (AEM) device for different groups, compared with IrO₂. (B) In-situ Raman spectra of FeCoNiMoBO₃ (Group-3).

TABLE S1. **Hyperparameters of Cond-CDVAE model used in this work.** Each element type is embedded by a vector of length 50. MLP_{zc} is a multi-layer perceptron for concatenated latent vector and condition embedding vector. DimeNet++ [56, 57] and GemNet-dQ [58] are used as PGNN_{Enc} and PGNN_{Dec} , respectively.

Model	Value
Element type embedding	50
vectorized PDM dimension	197
MLP_{zc} number of layers	3
MLP_{zc} number of hidden channels	64
MLP_L number of layers	1
MLP_L number of hidden channels	256
PGNN_{Enc} number of blocks	4
PGNN_{Enc} number of hidden channels	128
PGNN_{Enc} interaction embedding size	128
PGNN_{Dec} number of blocks	4
PGNN_{Dec} number of hidden channels	128
Loss weight λ_L	10
Loss weight λ_X	10
Loss weight β	0.01
Optimizer	Value
Optimizer type	Adam
Learning rate	1e-4
Learning rate scheduler	ReduceLROnPlateau
Scheduler patience (epoch)	30
Scheduler factor (epoch)	0.6
Minimal learning rate	1e-5
Data	Value
Batch size	128

TABLE S2. **Elemental compositions of catalysts estimated from ICP and element analysis.** Metallic contents were determined by ICP, and O contents were detected by difference subtraction of mass conservation.

Catalyst	Fe (mol %)	Co (mol %)	Ni (mol %)	Mo (mol %)	B (mol %)	O (mol %)
Group-1	8.74	8.23	8.26	6.93	5.87	61.98
Group-2	9.02	8.65	8.62	6.45	8.47	58.79
Group-3	10.36	10.03	9.94	7.23	11.68	50.76